






RESEARCH ARTICLE | FEBRUARY 06 2023

Experimental investigation of the effect of sectional airfoil profile deviation on propeller noise

Han Wu (吴翰) ; Wangqiao Chen (陈望桥) ; Hanbo Jiang (姜汉博) ; Siyang Zhong (钟思阳) ; Xin Zhang (张欣) 



Physics of Fluids 35, 027104 (2023)

<https://doi.org/10.1063/5.0135555>



View
Online



Export
Citation

Articles You May Be Interested In

Experimental investigation of trailing edge noise from stationary and rotating airfoils

J. Acoust. Soc. Am. (May 2017)

Study on flow-induced noise propagation mechanism of cylinder–airfoil interference model by using large eddy simulation combined with vortex–acoustic equation

AIP Advances (March 2023)

Inflow turbulence distortion for airfoil leading-edge noise prediction for large turbulence length scales for zero-mean loading

J. Acoust. Soc. Am. (March 2023)



Physics of Fluids

Special Topics Open for Submissions

[Learn More](#)

Experimental investigation of the effect of sectional airfoil profile deviation on propeller noise

Cite as: Phys. Fluids **35**, 027104 (2023); doi: [10.1063/5.0135555](https://doi.org/10.1063/5.0135555)

Submitted: 21 November 2022 · Accepted: 17 January 2023 ·

Published Online: 6 February 2023



View Online



Export Citation



CrossMark

Han Wu (吴翰),¹  Wangqiao Chen (陈望桥),¹  Hanbo Jiang (姜汉博),²  Siyang Zhong (钟思阳),^{3,a)}  and Xin Zhang (张欣)^{1,4,a)} 

AFFILIATIONS

¹Department of Mechanical and Aerospace Engineering, The Hong Kong University of Science and Technology, Clear Water Bay, Kowloon, Hong Kong, China

²Eastern Institute for Advanced Study, Yongri Institute of Technology, Ningbo, Zhejiang 315201, China

³Department of Aeronautical and Aviation Engineering, The Hong Kong Polytechnic University, Hung Hom, Kowloon, Hong Kong, China

⁴HKUST-Shenzhen Research Institute, Hi-Tech Park, Nanshan, Shenzhen 518057, China

^{a)}Authors to whom correspondence should be addressed: siyang.zhong@polyu.edu.hk and aexzhang@ust.hk

ABSTRACT

The geometry of the sectional airfoil has a determinative impact on the aeroacoustic characteristics of propellers. However, there are always slight deviations in the practical profiles due to manufacturing tolerance, wear loss, and limitations of processing techniques, which can potentially introduce uncertainties to aeroacoustic measurements. To this end, a systematic investigation is conducted on a benchmark propeller with a diameter of 217.2 mm and several of its variants in an anechoic wind tunnel. The variants are redesigned by modifying the sectional airfoil shapes with varying finite trailing-edge thicknesses. High-accuracy computer numerical control machining is employed to ensure the subtle geometrical differences between the blades. Force measurements indicate that the aerodynamic performances are insensitive to the slight variations of the sectional geometry, as expected. As for the acoustic performance, both the tonal and broadband noise are slightly affected when the axial flow speed is lower than 5 m/s. By contrast, a discernible noise reduction above 3 dB can be achieved due to the finite trailing-edge thickness. The noise source features are also investigated using a wavelet-based beamforming method, confirming that the noise reduction is caused by the weakened trailing-edge noise around the tip. This study is beneficial for the quantification of uncertainties in propeller noise measurements. It also suggests that adjusting trailing-edge thickness might be an useful approach in reducing propeller noise in practical applications.

Published under an exclusive license by AIP Publishing. <https://doi.org/10.1063/5.0135555>

I. INTRODUCTION

Small-size drones are ubiquitous in a wide spectrum of industrial applications, including photography,¹ detection,² rescue,^{3,4} and remote sensing.⁵ The most widely employed propulsive systems for drones are propeller-based ones since they can provide flexibility and maneuverability in flights. The noise issue could pose constraints to the future growth of the industry as drones generally operate in populated urban areas. The noise of drones is more likely to cause annoyance to human beings in the urban region.^{6,7}

The propeller aerodynamic noise is the primary noise source of drones, which is caused by the periodic motion of propeller blades.⁸

Recently, a number of experimental studies were made to characterize the noise radiated by drone propellers based on measurements in anechoic facilities.^{9–22} The noise measurements of the hovering propellers^{11–13} showed that the propeller noise was dominated by the harmonics of the blade pass frequency (BPF) below 1000 Hz, while the broadband trailing-edge noise was dominant at higher frequencies. Measurements were also conducted in the anechoic wind tunnels to characterize the propeller noise under different flight conditions. A wind tunnel measurement showed that the broadband noise could be increased by reducing the shaft angle for a propeller under forward flight.¹⁶ The measurement results by Grande *et al.*^{18,19} suggested that

TABLE I. Comparison of materials and manufacturing methods of propeller models used in recent aeroacoustic experiments.

Author and year	Material	Manufacturing method
Ning and Hu (2016) ^{11,12}	Resin	Additive manufacturing
Zawodny <i>et al.</i> (2016) ¹³	Glass fiber composite	Mold injection
Fattah <i>et al.</i> (2019) ¹⁴	Aluminum alloy	CNC machining
Yang <i>et al.</i> (2020) ¹⁶	Aluminum alloy	CNC machining
Pettingill <i>et al.</i> (2021) ¹⁷	ABS and mineral-filled nylon	Additive manufacturing
Grande <i>et al.</i> (2021) ^{18,19}	Aluminum alloy	CNC machining
Moslem <i>et al.</i> (2022) ²⁰	Polylactic acid	Additive manufacturing
Hanson <i>et al.</i> (2022) ²¹	Plastics	Additive manufacturing

the significant broadband noise corresponded to the laminar separation on the blade surface.

For experiments, one issue that could affect the results is the quality of the testing model. Table I compares the materials and manufacturing methods of several recent studies. In some studies,

computer numeric control (CNC) machining was adopted to manufacture metal propellers, where high accuracy can be achieved. However, in practice, the commercial off-the-shelf propeller blades are generally manufactured through mold injection, for which the accuracy is limited (the variation can vary from 0.1 to 0.7 mm). Custom-designed propellers can also be made by additive manufacturing (AM), also known as 3D printing.^{10–12,17,20,21} In the AM processes, the 3D printer nozzle builds the blade models layer by layer along the chordwise direction, as shown in Fig. 1(a), which can enable a smooth airfoil definition. However, some factors can limit the accuracies of AM products, leading to dimensional and shape deviations from their nominal geometries.^{23,24} Figure 1(b) presents a sectional view of the AM process. The airfoil is built from the leading edge and formed by multiple layers. Each layer has a specific limit on its thickness to provide a solid support for the product. Generally, the dimensional tolerances of common AM methods fall into the range of 0.05–0.20 mm,²⁴ making it challenging to manufacture the sharp trailing edge. Therefore, the dimensional tolerance of AM could result in shape deviations of the airfoil, especially in the trailing-edge region.

The geometrical change in the blade trailing edge can affect the noise generation. As demonstrated in Fig. 1(c), the local boundary conditions change rapidly when turbulence passes the blade trailing edge, and, thus, significant sound can be generated.²⁵ There are a lot of efforts on noise mitigation by applying add-on structures on the airfoil, such as velvet surface treatment,^{26,27} leading-edge serrations,²⁸ and flexible trailing fringe structures.^{29,30} Liu and Lee³¹ studied the effects of various geometrical parameters on trailing-edge noise,

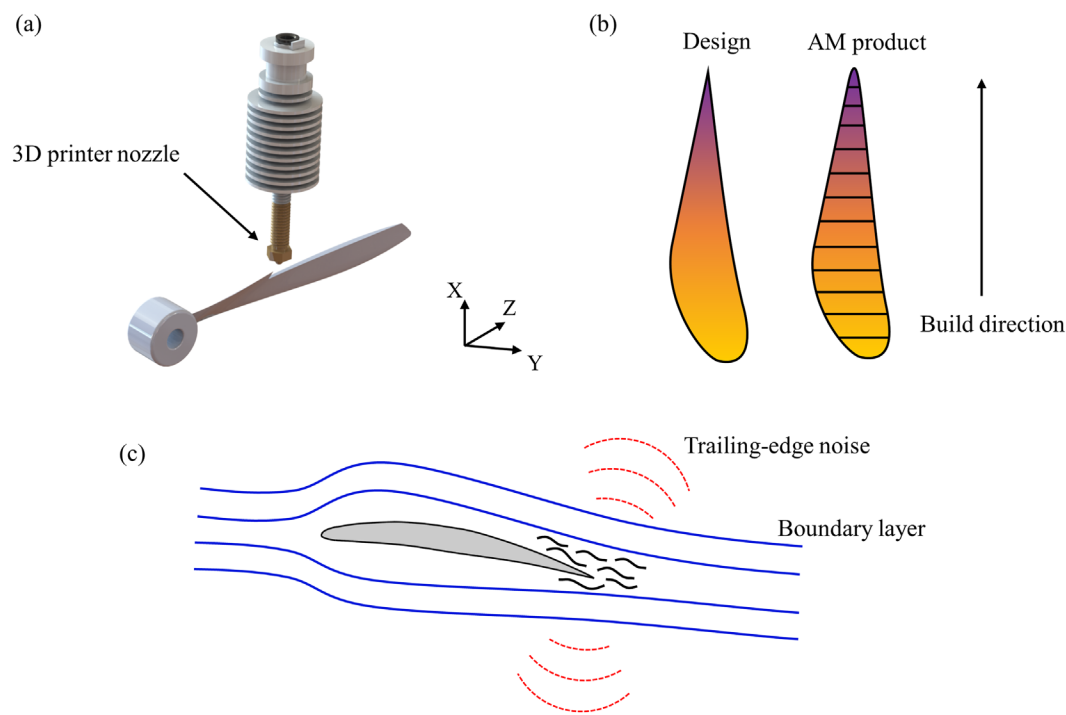


FIG. 1. Problem statement: (a) Demonstration of the manufacturing process of propeller models. The nozzle of the 3D printer builds the blade models along the X axis layer-wise. (b) The sectional view of the manufacturing process. For each blade section, the airfoil is built from the leading edge to the trailing edge. The dimensional tolerance of each layer can lead to shape deviations near the trailing edge. (c) Schematic of the blade trailing-edge noise.

including the trailing-edge thickness, the camber crest point, and leading-edge radius.³¹ However, there are rare works focusing on the effect of airfoil shape on propeller noise.

In this work, we conduct an experimental study to assess the effect of airfoil on propeller noise, where different shapes are controlled by high-accuracy CNC machining. The geometrical changes in the blade trailing edge are fairly small, such that the results can lead to an insight into the potential influence of manufacturing tolerance in practice. Aeroacoustic measurements are conducted in an anechoic wind tunnel, and the aerodynamic and acoustic performances under different working conditions are compared.

The remaining part of this paper is organized as follows. The experimental setup is described in Sec. II, including the propeller design and the test environment. The measurement uncertainties in experiments are quantified in Sec. III. Then, aerodynamic and acoustic results are presented and discussed in Sec. IV. A summary is given in Sec. V.

II. EXPERIMENTAL SETUP

A. Propeller design

In this work, a low-noise propeller SP2 developed at HKUST was used as a baseline configuration.³² The propeller has two blades with a diameter of 217.2 mm. The chord length and pitch angle distribution along the radial direction (r/R , normalized by radius) are shown in Fig. 2.

The original design of SP2 employed a NACA4412 airfoil as the sectional profile along the entire blade. A comparison of original and redesigned airfoils is demonstrated in Fig. 3, where X and Y denote the chordwise direction and the thickness-wise direction, respectively. The modified airfoil can maintain the camber line and camber crest point as the original airfoil, and the leading-edge radius is unaffected. In this work, the trailing-edge thickness (B) of NACA4412 is increased to indicate the geometrical changes likely existing in additive manufacturing due to the dimensional tolerance.³³ Three modified shapes of NACA4412 were used in this work to conduct a parametric study. The non-dimensional trailing-edge thickness B/C for each shape was 1%, 2%, and 3%, where C denotes the chord of the sectional airfoil. The propeller models were, thus, labeled as SP2B1, SP2B2, and SP2B3. The propellers, made of aluminum alloys, were manufactured by CNC machining with an accuracy of $25\text{ }\mu\text{m}$, which can guarantee delicate shape deviations.

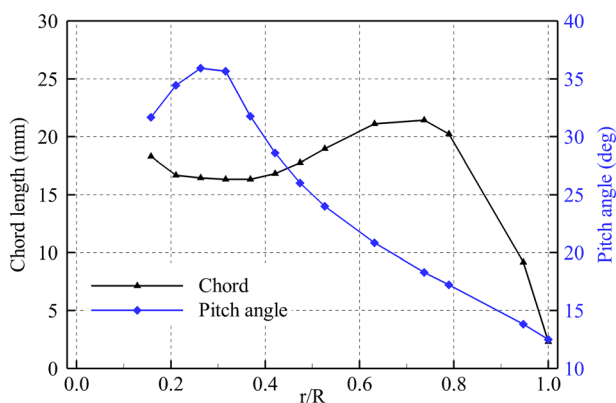


FIG. 2. The radial chord and pitch angle distributions of the propeller SP2.

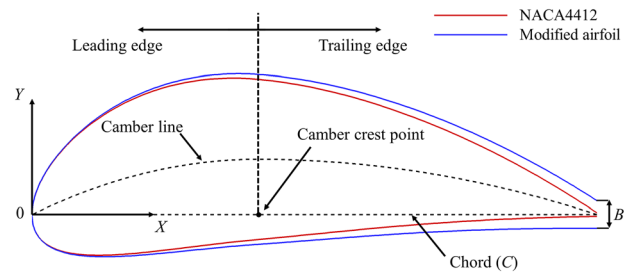


FIG. 3. The comparison of the original airfoil (NACA4412) and a demonstration of the modified airfoils.

B. Experimental platform

The aeroacoustic measurements were performed in the rotor aeroacoustics test platform at HKUST.¹⁵ The test platform is installed in a wind tunnel with the working section enclosed by an anechoic chamber of $3.3\text{ (length)} \times 3.1\text{ (width)} \times 2.0\text{ m}^3\text{ (height)}$. The chamber has an open-jet inflow duct of $0.4 \times 0.4\text{ m}^2$ and a jet collector to facilitate the flow. The internal structure of the collector is acoustically treated to mitigate the sound reflection for acoustic measurements.³⁴

The rotor test rig can perform synchronized measurements of the rotational speed, aerodynamic loading, and noise. The control of rotational speed is based on the feedback from an electrical speed controller, which receives the command of the pulse width modulation. The rotational speed is measured by an optical rotary encoder attached to the back end of the motor shaft. The rotary encoder outputs 100 pulses per revolution, and the statistical rotational speed can be obtained every 0.02 s. A load cell with six degrees of freedom is employed to capture relevant aerodynamic loading. The sensing range is 120 N in the direction of the propeller thrust, with the resolution of 1/50 N. For the torque, the sensing range is 2 N m with a resolution of 1/4000 N m. The sampling frequency for the aerodynamic force and torque is 20 kHz. A phase microphone array containing 56 Brüel & Kjær type 4957 free-field microphones is implemented to measure the far-field noise radiation of the propeller. The data obtained from the phased microphone array are also used for sound source imaging computation based on beamforming techniques. The microphones are installed on seven spiral arms, and the schematic is shown in Fig. 4(a). The microphone array is placed 0.8 m on the side of the test rig. The center of array is aligned with the propeller. The sampling frequency for noise data is 50 kHz. The sampling time for each measurement is 10 s. A schematic of the experimental setup is given in Fig. 4(b). All the metallic materials are covered with sound-absorbing foam to minimize the sound reflection during experiments.

Welch's method³⁵ for Power Spectral Density (PSD) estimation was used to transform the time-domain noise signals into the frequency-domain spectra. The time-series data were divided into 100 data blocks with a 50% overlap. Each block consisting of 10 000 data points was pre-processed by a Hanning window function, leading to a frequency resolution of 10 Hz. A wavelet-based beamforming method was implemented to estimate the noise source distribution on the rotational plane.^{36–38} The novel beamforming method was developed for high-speed rotational objects and has been validated by numerical simulations and experiments by prior works.³⁶

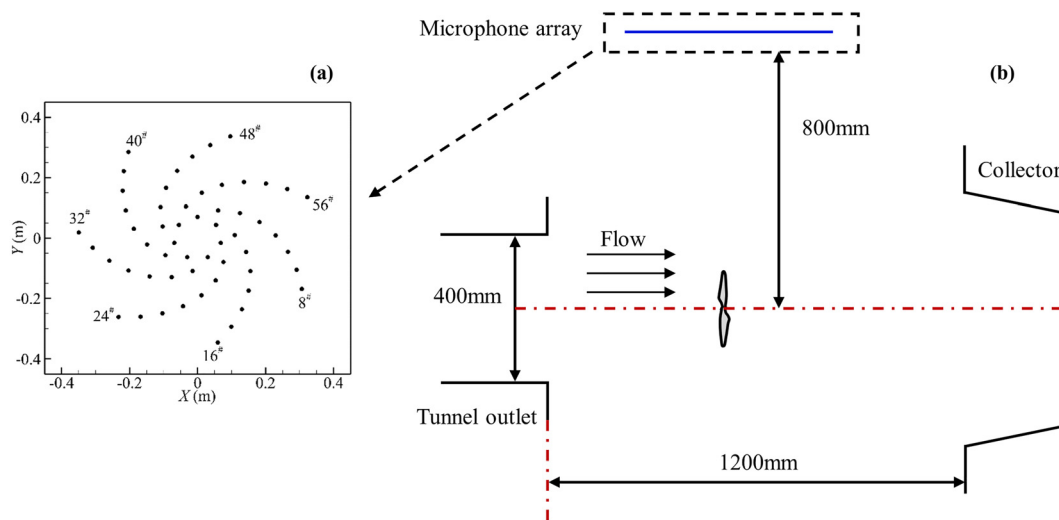


FIG. 4. The experimental setup: (a) The schematic of the phase microphone array; (b) The schematic of the experiment setup. The test rig and the jet collector are acoustically treated to reduce the sound reflection in acoustic measurement.

C. Experimental test matrix

The experiments were conducted under conditions of hovering (zero flow speed) and axial climbing (axial advancing flow). The tested rotational speed varied from 40 to 120 revolutions per second (RPS) at an interval of 5 RPS, which provides sufficient aerodynamic and acoustic data. The propellers were tested under different axial advancing flow speeds up to 10 m/s. In this work, the 0 (hover), 5, and 10 m/s cases are used for clarity.

III. EXPERIMENTAL UNCERTAINTIES

In this work, the variation of B/C is small. To avoid misinterpretation of the measurement results, it is necessary to have the uncertainties well identified and controlled.

A. Background and motor noise

The narrow-band noise spectra of propeller SP2 under different working conditions are compared with the isolated motor noise and the facility background noise in Fig. 5. The noise data were measured by the microphone at the rotational plane. The propeller emits tonal

noise at the BPF and its harmonics, while the broadband noise is the dominant component in the high-frequency range. As shown in Fig. 5, the background noise increases with the freestream U_∞ , especially at the frequency range under 1000 Hz. The propeller noise is dominated by the high-level BPF tones below 1000 Hz, and the broadband trailing-edge noise is more than 10 dB higher than the background noise over the entire frequency range. The electric motor generates discrete tones near $14 \times$ RPS and $42 \times$ RPS, which is attributed to structural vibration of the motor.^{15,39} The comparison indicates the good signal to noise ratio of the acoustic measurement from 100 to 20 000 Hz.

B. Uncertainty analysis of force and noise measurement

The total force measurement uncertainty (σ) is often contributed by different sources, as given by

$$\sigma = \sqrt{\sigma_r^2 + \sigma_s^2}, \quad (1)$$

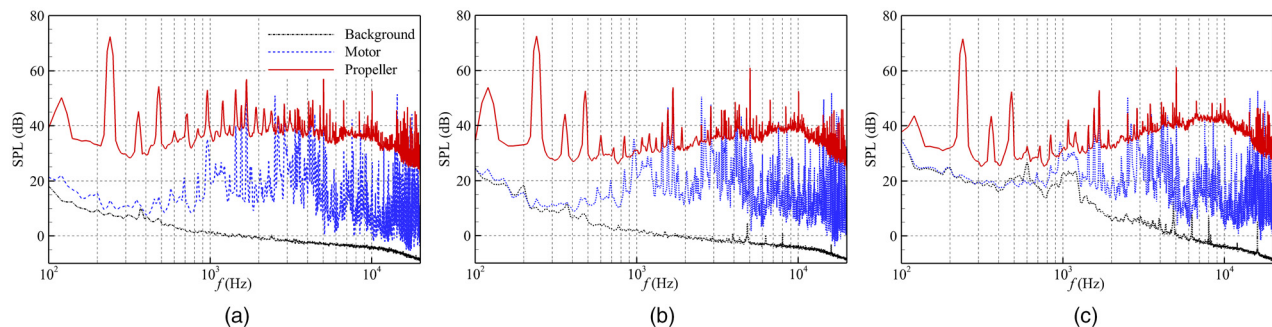


FIG. 5. Comparison between propeller noise and background/motor noise under various axial flow speeds. The propeller is working at 120 RPS. (a) $U_\infty = 0$ m/s, (b) $U_\infty = 5$ m/s, and (c) $U_\infty = 10$ m/s.

TABLE II. A summary of the uncertainty contributions for force measurement.

Source	Thrust (N)	Torque (N mm)
Systematic uncertainty	0.011	0.470
Random uncertainty	0.083	0.736
Total uncertainty	0.084	0.873

where σ_r and σ_s denote the random uncertainty and systematic uncertainty, respectively.⁴⁰

The systematic uncertainty σ_s is quantified by the force shift due to wind loading on the test rig structure. The maximum shifts of thrust and torque are recorded for conservative purposes, and the values are 0.011 N and 0.470 N mm, respectively. The random uncertainty σ_r mainly considers the repeatability of the force measurements. The uncertainties of the thrust and torque measurements based on the repeatability tests at the 95% confidence interval are 0.083 N and 0.736 N mm, respectively. The uncertainty sources and the total uncertainty for thrust and torque are summarized in Table II.

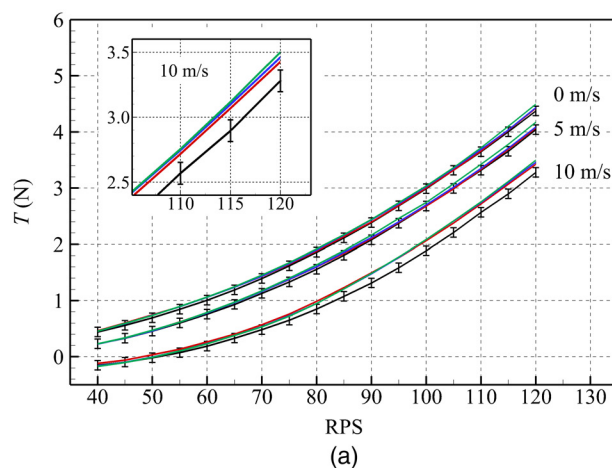
For the acoustic results, in this work, we mainly focus on the random uncertainty using the repeatability tests of the baseline propeller SP2 on different dates. The sound pressure level (SPL) of tonal noise at the BPF and the overall sound pressure level of broadband noise (OASPL_{bbn}, 1000–20 000 Hz) are used for uncertainty analysis. The corresponding uncertainties at the 95% confidence interval are 0.33 and 0.76 dB based on the t -distribution.⁴¹

IV. RESULTS AND DISCUSSION

A. Aerodynamic performance

The averaged thrust T and torque Q are computed based on the sampling results of the load cell during a period of 10 s. Thrust coefficient C_T , power coefficient C_P , and the propeller's figure of merit FM are then defined according to Ref. 42 as

$$C_T = \frac{T}{\rho A (\Omega R)^2}, \quad C_P = \frac{P}{\rho A (\Omega R)^3}, \quad FM = \frac{C_T^{3/2}}{\sqrt{2} C_P}, \quad (2)$$



where $\Omega = 2\pi \cdot \text{RPS}$ is the angular frequency in rad/s, $P = Q \cdot \Omega$ is the propeller power, ρ is the air density, $A = \pi R^2$ is the rotor disk area, and R is the blade radius.

Figure 6 shows the measured aerodynamic results under varying axial flow speeds. The uncertainties of the thrust and torque are indicated by the error bars, which have been discussed in Sec. III. In general, the thrust of all the propellers drops with increasing axial flow speed, as the effective angle of attack of the propeller is reduced. It can be seen from Fig. 6(a) that at the flow speed of 0 and 5 m/s, the thrust of propeller SP2 is nearly identical with the modified shapes at the rotational speeds tested. While under the high advancing flow of 10 m/s, the modified propellers can retain a higher thrust level than the baseline propeller SP2 [see the zoom-in view of Fig. 6(a)].

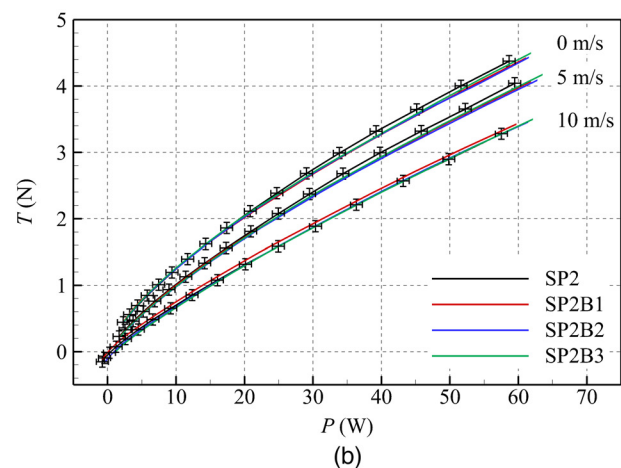
The power consumption is also plotted against the thrust as shown in Fig. 6(b). It can be seen that increasing the trailing-edge thickness will also increase power, while the thrust is enhanced. The geometrical changes due to dimensional tolerance of AM processes could induce more thrust and power (torque) at the same time. In general, the thrust-to-power curves collapse well for all the flow conditions, indicating the thrust-to-power trends for all propellers are similar.

The FM curves for all propellers are compared to demonstrate the aerodynamic efficiency under hovering conditions. The figure of merit is defined by the ratio of ideal power to the actual power of a hovering propeller/rotor to indicate its efficiency.⁴² Figure 7(a) shows that the FM curves collapse reasonably for the propellers at the hovering state, suggesting the propellers possess similar aerodynamic efficiency. The thrust coefficient of all propellers can remain at a nearly constant level over the testing range at 0 and 5 m/s as shown in Fig. 7(b). For $U_\infty = 10$ m/s, the thrust coefficient is slightly changed with the increase in B .

B. Acoustic characteristics

1. Influence of rotational speed and flow speed

The SPL of the primary tone is plotted against the varying rotational speeds and axial flow speeds, as shown in Fig. 8. The noise


FIG. 6. The averaged thrust and power comparison of the propellers. (a) Thrust versus speed and (b) Thrust versus power.

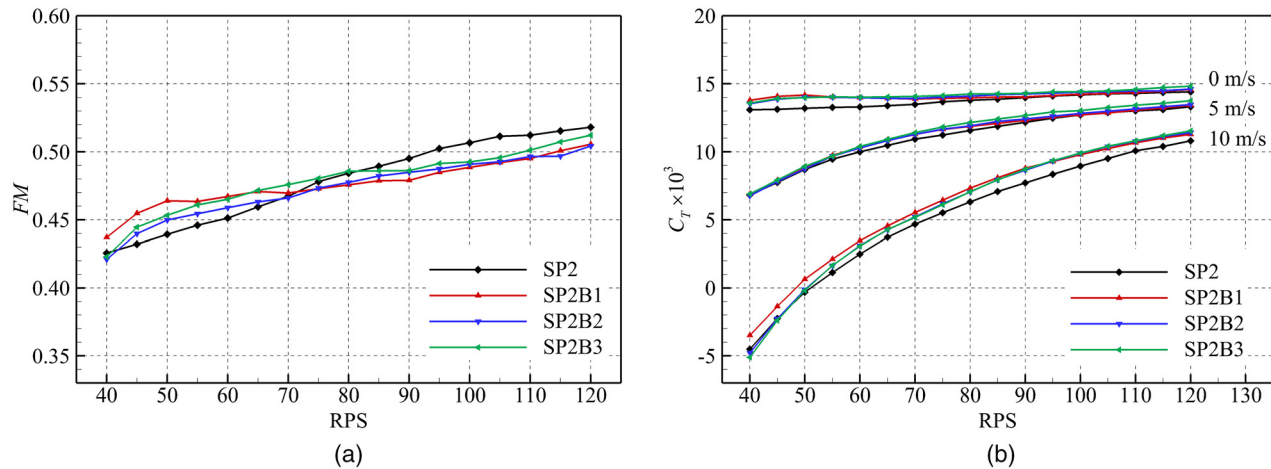


FIG. 7. The non-dimensional coefficients comparison of the propellers. (a) Figure of merit and (b) Thrust coefficient.

measurement uncertainties analyzed in Sec. III are indicated by error bars. For small-scale rotors, the tonal noise at the BPF mainly depends on the steady aerodynamic loading on the blade surface.⁴³ Thus, the results of the three modified propellers at the static flow are close. By contrast, as the axial flow speed increases, the thrusts of SP2B1, SP2B2, and SP2B3 become slightly higher than SP2 (see Fig. 6), such that a discernible increase in the SPLs at the BPF can be observed. However, the overall differences in the tonal noise of the three blades are minor. In general, Fig. 8 demonstrates that all the propellers exhibit similar growth patterns on the BPF tonal noise.

In this work, the effect of the airfoil geometry deviation on the broadband noise is also studied by extracting broadband contents from the narrow band spectra using a local regression method.^{14,15} The $OASPL_{bbn}$ is estimated by integrating the acoustic energy from 1000 to 20 000 Hz. The comparisons of $OASPL_{bbn}$ under various flow speeds are shown in Fig. 9. In general, the $OASPL_{bbn}$ for all the propellers increases with rotational speed fairly evenly. The $OASPL_{bbn}$ of SP2 is slightly lower than the others at the static flow, as SP2 can maintain a better hovering efficiency [see Fig. 7(a)]. Generally, the broadband noise levels are close for the 0 and 5 m/s cases, but the propellers exhibit different broadband characteristics at 10 m/s. The baseline configuration SP2 generates more significant broadband noise when the

rotational speed exceeds 90 RPS. An increase in $OASPL_{bbn}$ over 3 dB can be observed in Fig. 9. As indicated by the force measurements in Fig. 7(b), SP2 suffers a loss of thrust coefficient at 10 m/s. Interestingly, it has the highest broadband noise level at this working condition, as shown in Fig. 9. The spectral properties are further analyzed to discuss the effect of the changes in trailing-edge thickness.

2. Spectral characteristics of broadband noise

The broadband noise spectra at 10 m/s are plotted against the rotational speed and the frequency f in Fig. 10. One can find a domain where the broadband noise is significant, as indicated by the black dashed lines. The lower bound of this domain is approximately $f = 5000$ Hz. The upper bound of this domain seems to vary with the rotational speed. In an attempt to represent the upper bound, f is non-dimensionalized as the Strouhal number (St), which is defined by

$$St = \frac{f \cdot C_{0.75}}{V_{0.75}}, \quad (3)$$

where $C_{0.75}$ denotes the chord length of the blade segment at the radial position of 75% radius and $V_{0.75}$ is the tangential velocity at 75%

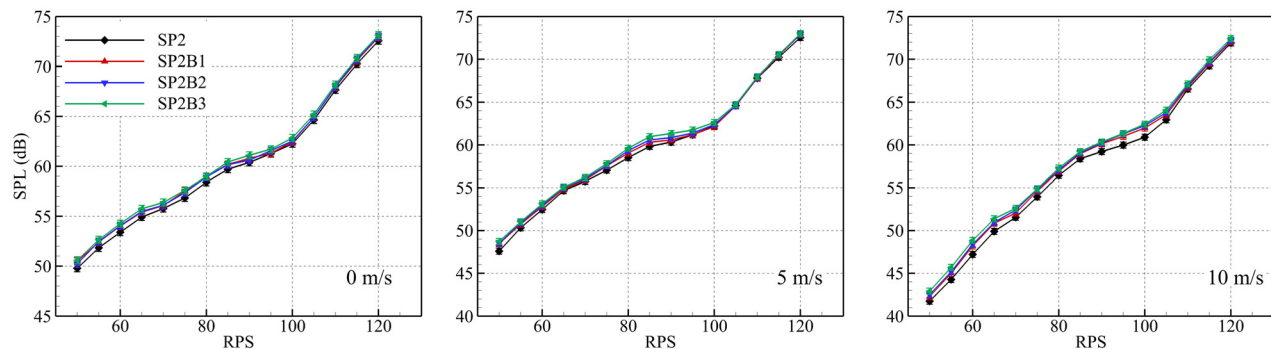


FIG. 8. Comparison of the BPF tonal noise for all the propellers. The noise data were obtained from a microphone at the rotational plane.

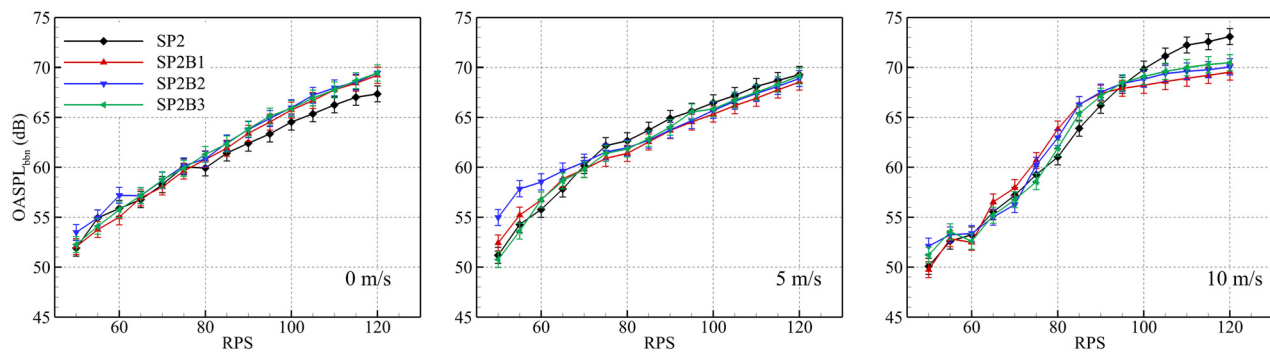


FIG. 9. OASPL_{bbn} comparison for all the propellers. The noise data were obtained from a microphone at the rotational plane.

radius. Then, the approximate domain upper boundary can be indicated by $St \approx 6.2$. The broadband noise of the modified propellers is notably less significant than the baseline propeller within the given domain.

The narrow-band and 1/3 octave band spectra of broadband noise at $U_\infty = 10$ m/s at different observer locations are shown in Fig. 11. The propellers were operated at 120 RPS to highlight the significance of broadband noise. The results obtained from microphones 1[#] and 56[#] are presented, showing similar spectral characteristics on and out of the rotational plane. The broadband noise of propeller SP2 is 3 dB higher than others, forming a hump in the high-frequency range of the spectrum. Similar spectral shapes of broadband noise

were also observed in experiments, which corresponded to the flow separation under high advance ratios.¹⁸ The high advance ratios (off-design points) can also lead to the degradation of propeller aerodynamic efficiency.^{44,45} The lower noise emissions of modified propellers suggest that the propeller noise potentially caused by flow separations at off-design points can be reduced by changing the airfoil geometry properly.

Figure 12 shows the effect of increasing the trailing-edge thickness B/C on propeller performances (at $U_\infty = 10$ m/s and 120 RPS). The aerodynamic coefficients C_T and C_P are compared in Fig. 12(a). These coefficients are scaled by the results of the baseline SP2. The trailing-edge thickness can increase the thrust and power coefficients

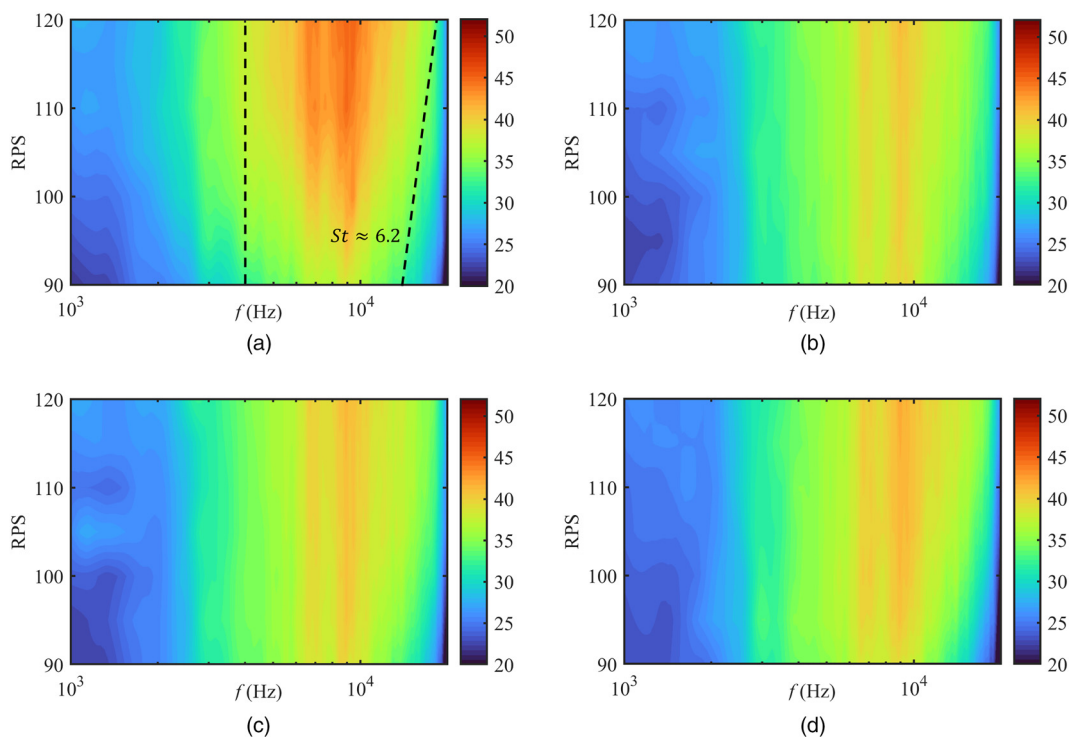


FIG. 10. The SPL contours comparison at $U_\infty = 10$ m/s. The noise data were obtained from a microphone at the rotational plane. (a) SP2, (b) SP2B1, (c) SP2B2, and (d) SP2B3.

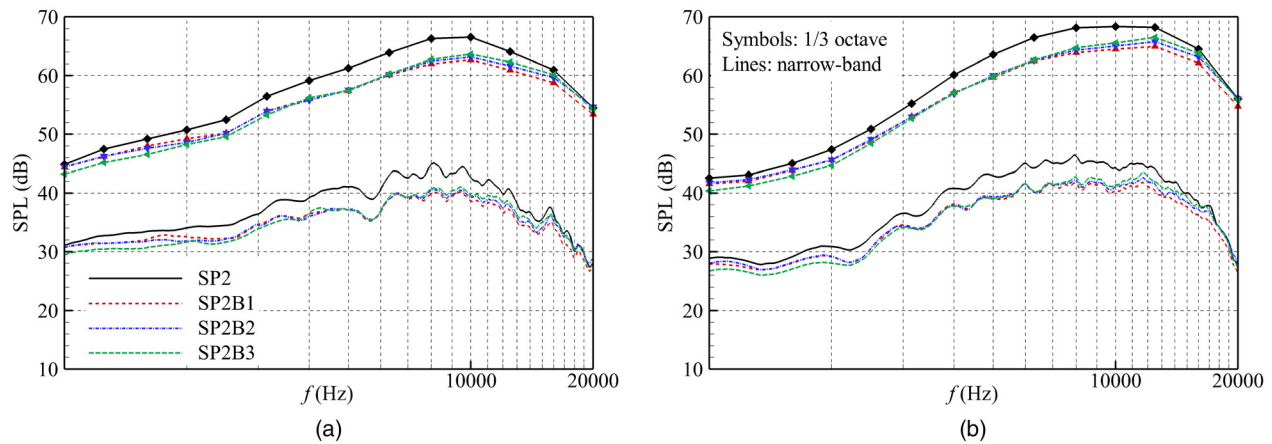


FIG. 11. The broadband noise spectra are compared for different locations. The data obtained out of the rotor plane retain the same pattern as data obtained from the rotational plane. (a) Microphone 1[#] and (b) Microphone 56[#].

at the same time. The broadband noise is divided into the mid-frequency (1000–5000 Hz) and high-frequency (5000–20 000 Hz) regions. The acoustic energies are integrated over these two regions and compared in Fig. 12(b). It can be seen that the geometrical changes in the airfoil shape can reduce the broadband noise emission at both the mid- and high-frequency ranges under $U_\infty = 10$ m/s.

C. Acoustic imaging results

As suggested by Fig. 12(d), the broadband noise is mainly contributed by the noise contents in the range between 5000 and 20 000 Hz. To illustrate the broadband source location, the wavelet-based beamforming method is employed. A representative frequency of 10 000 Hz is selected as the broadband noise is dominant at this frequency, and a relatively high resolution of the acoustic imaging can be achieved. The method can capture the transient variations of the propeller noise source.^{36–38} The comparison of beamforming results is

shown in Fig. 13 to indicate the source distribution at different advanced flow speeds.

The white dashed circle in Fig. 13 represents the tip of the propeller for illustrative purposes. The corresponding source location is around the tip of the propeller blades, as shown in Fig. 13. The tip region is crucial for propeller noise, where significant flow interaction with the trailing edge occurs. The importance of tip regions was also highlighted by previous beamforming investigations of rotating blades.^{37,38,46,47} For the cases of 0 and 5 m/s, there are negligible differences in source strength between the tested propellers, which is in line with the results in Fig. 9. However, at 10 m/s, the source strength of propeller SP2 is fairly recognizable compared to modified propellers, indicating the changes in airfoil can influence the generation of trailing-edge noise.

The motor noise can also be observed around the center of the propeller disk under some working conditions, which has also been found in previous propeller aeroacoustic measurements.^{37,38} In this

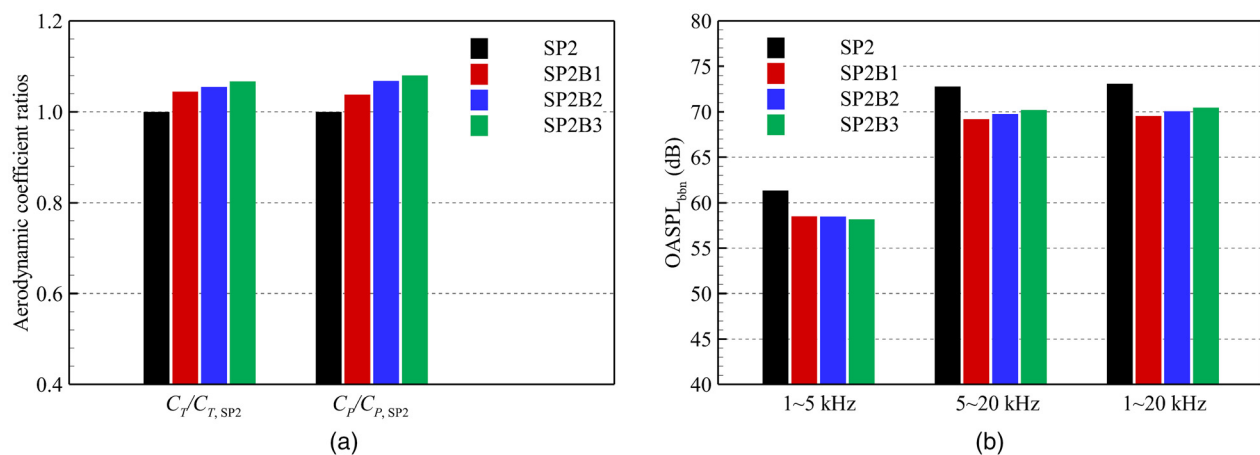


FIG. 12. Effects of the change in airfoil shape on aerodynamic and acoustic performances. (a) Aerodynamic performance and (b) Noise levels at different frequencies.

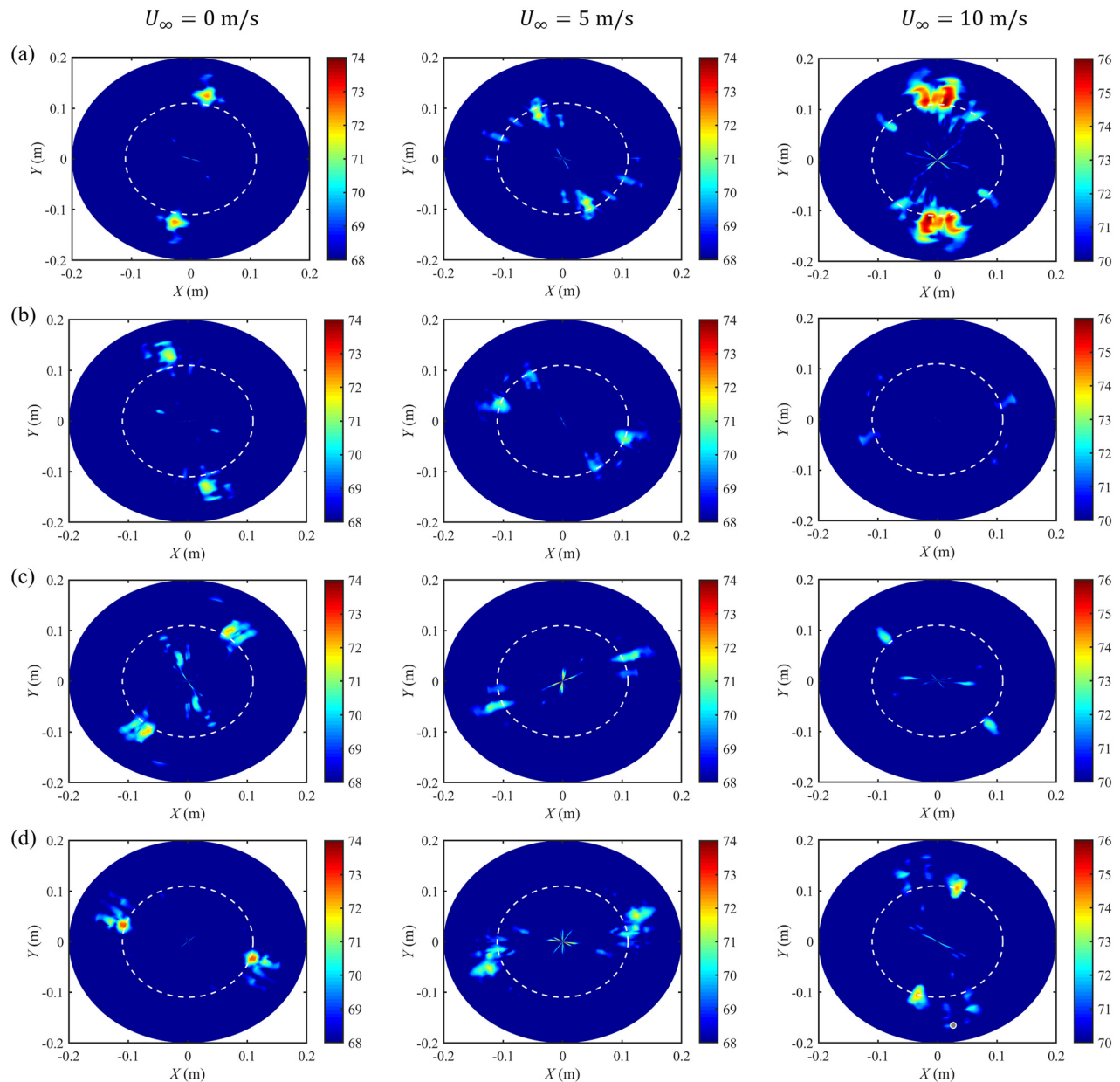


FIG. 13. Acoustic imaging results at $f = 10\,000$ Hz for various propellers under different flow speeds: (a) SP2, (b) SP2B1, (c) SP2B2, and (d) SP2B3. The rotational speed is 120 RPS.

work, the strength of motor noise is less significant at the frequency of interest as discussed in Fig. 5. Hence, the beamforming results can reveal the source strength of the dominated broadband noise.

V. SUMMARY

In this work, we described an experimental study on the effect of shape deviations of the sectional airfoil of drone propellers. The geometrical changes are due to the dimensional tolerance of AM processes, which are often adopted to produce propeller models for

experiments. To indicate the subtle shape deviations, the blade sections were designed with varying finite trailing-edge thicknesses and manufactured with high-accuracy CNC machining. The aerodynamic force measurements show negligible effect due to geometrical deviations. The differences of tonal noise and $OASPL_{bbn}$ are slight at $U_\infty = 0$ and 5 m/s. By contrast, a discernible noise reduction of 3 dB can be observed under the axial flow of 10 m/s, indicating the potential noise reduction due to the finite trailing-edge thickness. A wavelet-based beamforming method is implemented to visualize the sound source

features. The acoustic imaging results reveal that noise reduction is achieved by the weakened trailing-edge noise source around the blade tip. The experimental observations show that the effect of geometrical changes in the airfoil shape is minor for aeroacoustic measurements. In addition, the potential trailing-edge noise reduction by adjusting the trailing-edge thickness might provide insights into the low-noise design of practical drone propellers.

ACKNOWLEDGMENTS

This work was supported by the Hong Kong Research Grant Council (Nos. RGC 16202520 and 16206422) and the National Natural Science Foundation of China (No. NSFC 11972029).

AUTHOR DECLARATIONS

Conflict of Interest

The authors have no conflicts to disclose.

Author Contributions

Han Wu: Conceptualization (equal); Data curation (lead); Formal analysis (lead); Investigation (lead); Methodology (equal); Software (lead); Writing – original draft (lead). **Wangqiao Chen:** Methodology (equal); Writing – review & editing (supporting). **Hanbo Jiang:** Formal analysis (supporting); Writing – review & editing (equal). **Siyang Zhong:** Conceptualization (equal); Supervision (supporting); Writing – review & editing (equal). **Xin Zhang:** Conceptualization (equal); Funding acquisition (lead); Project administration (lead); Resources (lead); Supervision (lead); Writing – review & editing (equal).

DATA AVAILABILITY

The data that support the findings of this study are available from the corresponding author upon reasonable request.

REFERENCES

- Colomina and P. Molina, “Unmanned aerial systems for photogrammetry and remote sensing: A review,” *ISPRS J. Photogramm. Remote Sens.* **92**, 79–97 (2014).
- N. H. Motlagh, M. Bagaa, and T. Taleb, “UAV-based IoT platform: A crowd surveillance use case,” *IEEE Commun. Mag.* **55**, 128–134 (2017).
- T. Tomic, K. Schmid, P. Lutz, A. Domel, M. Kassecker, E. Mair, I. L. Grixia, F. Ruess, M. Suppa, and D. Burschka, “Toward a fully autonomous UAV: Research platform for indoor and outdoor urban search and rescue,” *IEEE Rob. Autom. Mag.* **19**, 46–56 (2012).
- M. A. Goodrich, J. L. Cooper, J. A. Adams, C. Humphrey, R. Zeeman, and B. G. Buss, “Using a mini-UAV to support wilderness search and rescue: Practices for human-robot teaming,” in *IEEE International Workshop on Safety, Security and Rescue Robotics* (IEEE, 2007), pp. 1–6.
- J. Xue and B. Su, “Significant remote sensing vegetation indices: A review of developments and applications,” *J. Sens.* **2017**, 1353691.
- A. W. Christian and R. Cabell, “Initial investigation into the psychoacoustic properties of small unmanned aerial system noise,” AIAA Paper No. 2017-4051, 2017.
- A. J. Torija, Z. Li, and R. H. Self, “Effects of a hovering unmanned aerial vehicle on urban soundscapes perception,” *Transp. Res., Part D* **78**, 102195 (2020).
- H. H. Hubbard, *Aeroacoustics of Flight Vehicles: Theory and Practice* (National Aeronautics and Space Administration, Office of Management, Scientific and Technical Information Program, 1991), Vol. 1.
- L. Marino, “Experimental analysis of UAV propeller noise,” AIAA Paper No. 2010-3854, 2010.
- G. Sinibaldi and L. Marino, “Experimental analysis on the noise of propellers for small UAV,” *Appl. Acoust.* **74**, 79–88 (2013).
- Z. Ning and H. Hu, “An experimental study on the aerodynamics and aeroacoustic characteristics of small propellers,” AIAA Paper No. 2016-1785, 2016.
- Z. Ning and H. Hu, “An experimental study on the aerodynamic and aeroacoustic performances of a bio-inspired UAV propeller,” AIAA Paper No. 2017-3747, 2017.
- N. S. Zawodny, D. D. Boyd, Jr., and C. L. Burley, “Acoustic characterization and prediction of representative, small-scale rotary-wing unmanned aircraft system components,” AHS Paper No. 20160009054, 2016.
- R. J. Fattah, W. Chen, H. Wu, Y. Wu, and X. Zhang, “Noise measurements of generic small-scale propellers,” AIAA Paper No. 2019-2498, 2019.
- H. Wu, W. Chen, R. Fattah, Y. Fang, S. Zhong, and X. Zhang, “A rotor blade aeroacoustics test platform at HKUST,” in *INTER-NOISE and NOISE-CON Congress and Conference Proceedings* (Institute of Noise Control Engineering, 2020), Vol. 261, pp. 2476–2484.
- Y. Yang, Y. Liu, Y. Li, E. Arcondoulis, and Y. Wang, “Aerodynamic and aeroacoustic performance of an isolated multicopter rotor during forward flight,” *AIAA J.* **58**, 1171–1181 (2020).
- N. A. Pettingill, N. S. Zawodny, C. Thurman, and L. V. Lopes, “Acoustic and performance characteristics of an ideally twisted rotor in hover,” AIAA Paper No. 2021-1928 (2021).
- E. Grande, G. Romani, D. Ragni, F. Avallone, and D. Casalino, “Aeroacoustic investigation of a propeller operating at low Reynolds numbers,” *AIAA J.* **60**, 860–871 (2022).
- E. Grande, D. Ragni, F. Avallone, and D. Casalino, “Laminar separation bubble noise on a propeller operating at low Reynolds numbers,” *AIAA J.* **60**, 5324–5335 (2022).
- F. Moslem, M. Masdari, K. Fedir, and B. Moslem, “Experimental investigation into the aerodynamic and aeroacoustic performance of bioinspired small-scale propeller planforms,” *Proc. Inst. Mech. Eng., Part G* **237**, 75–90 (2022).
- L. P. Hanson, K. Baskaran, S. F. Pullin, B. Y. Zhou, B. Zang, and M. Azarpeyvand, “Aeroacoustic and aerodynamic characteristics of propeller tip geometries,” AIAA Paper No. 2022-3075, 2022.
- H. Wu, H. Jiang, P. Zhou, S. Zhong, X. Zhang, G. Zhou, and B. Chen, “On identifying the deterministic components of propeller noise,” *Aerosp. Sci. Technol.* **130**, 107948 (2022).
- G. Ameta, P. Witherell, S. Moylan, and R. Lipman, “Tolerance specification and related issues for additively manufactured products,” in *International Design Engineering Technical Conferences and Computers and Information in Engineering Conference* (American Society of Mechanical Engineers, 2015), Vol. 57045.
- P. Minetola, F. Calignano, and M. Galati, “Comparing geometric tolerance capabilities of additive manufacturing systems for polymers,” *Addit. Manuf.* **32**, 101103 (2020).
- S. Glegg and W. Devenport, *Aeroacoustics of Low Mach Number Flows: Fundamentals, Analysis, and Measurement* (Academic Press, 2017).
- P. Zhou, S. Zhong, and X. Zhang, “On the effect of velvet structures on trailing edge noise: Experimental investigation and theoretical analysis,” *J. Fluid Mech.* **919**, A11 (2021).
- P. Zhou, S. Zhong, X. Li, Y. Li, W. Chen, H. Jiang, and X. Zhang, “Broadband trailing edge noise reduction through porous velvet-coated serrations,” *Phys. Fluids* **34**, 057112 (2022).
- J. Rong and H. Liu, “Effects of owl-inspired leading-edge serrations on tandem wing aeroacoustics,” *AIP Adv.* **12**, 115103 (2022).
- P. Zhou, Q. Liu, S. Zhong, Y. Fang, and X. Zhang, “A study of the effect of serration shape and flexibility on trailing edge noise,” *Phys. Fluids* **32**, 127114 (2020).
- Z. Deng, W.-L. Chen, and Z. Yang, “The control mechanism of the soft trailing fringe on the flow characteristics over an airfoil,” *Phys. Fluids* **34**, 095112 (2022).
- C. Liu and S. Lee, “Parametric airfoil design and sensitivity analysis for turbulent boundary-layer trailing-edge noise reduction,” *AIAA J.* **60**, 2324–2341 (2021).
- H. Jiang, H. Wu, W. Chen, P. Zhou, S. Zhong, X. Zhang, G. Zhou, and B. Chen, “Toward high-efficiency low-noise propellers: A numerical and experimental study,” *Phys. Fluids* **34**, 076116 (2022).

- ³³M. Drela, "Elements of airfoil design methodology," *Appl. Comput. Aerodyn.* **125**, 167–189 (1990).
- ³⁴W. Yi, P. Zhou, Y. Fang, J. Guo, S. Zhong, X. Zhang, X. Huang, G. Zhou, and B. Chen, "Design and characterization of a multifunctional low-speed anechoic wind tunnel at HKUST," *Aerosp. Sci. Technol.* **115**, 106814 (2021).
- ³⁵P. Welch, "The use of fast Fourier transform for the estimation of power spectra: A method based on time averaging over short, modified periodograms," *IEEE Trans. Audio Electroacoust.* **15**, 70–73 (1967).
- ³⁶W. Chen and X. Huang, "Wavelet-based beamforming for high-speed rotating acoustic source," *IEEE Access* **6**, 10231–10239 (2018).
- ³⁷W. Chen, B. Peng, R. P. Liem, and X. Huang, "Experimental study of airfoil-rotor interaction noise by wavelet beamforming," *J. Acoust. Soc. Am.* **147**, 3248–3259 (2020).
- ³⁸W. Chen, Z. Yang, B. Peng, and X. Huang, "On trailing edge noise from propellers with interactions to shear layers," *J. Sound Vib.* **495**, 115901 (2021).
- ³⁹D. L. Huff and B. S. Henderson, "Electric motor noise for small quadcopters—Part 1: Acoustic measurements," AIAA Paper No. 2018-2952, 2018.
- ⁴⁰J. B. Barlow, W. H. Rae, and A. Pope, *Low-Speed Wind Tunnel Testing* (Wiley, 1999).
- ⁴¹R. V. Hogg and A. T. Craig, *Introduction to Mathematical Statistics* (Springer Science & Business Media, Englewood Hills, NJ, 1995).
- ⁴²G. J. Leishman, *Principles of Helicopter Aerodynamics* (Cambridge University Press, 2006).
- ⁴³S. Zhong, P. Zhou, R. Fattah, and X. Zhang, "A revisit of the tonal noise of small rotors," *Proc. R. Soc. A* **476**, 20200491 (2020).
- ⁴⁴J. Brandt and M. Selig, "Propeller performance data at low Reynolds numbers," AIAA Paper No. 2011-1255, 2011.
- ⁴⁵R. W. Deters, G. K. Ananda Krishnan, and M. S. Selig, "Reynolds number effects on the performance of small-scale propellers," AIAA Paper No. 2014-2151, 2014.
- ⁴⁶C. Horváth, "Beamforming investigation of dominant counter-rotating open rotor tonal and broadband noise sources," *AIAA J.* **53**, 1602–1611 (2015).
- ⁴⁷B. Fenyvesi, J. Kriegseis, and C. Horváth, "An automated method for the identification of interaction tone noise sources on the beamforming maps of counter-rotating rotors," *Phys. Fluids* **34**, 047105 (2022).